Transcranial photoacoustic characterization of neurovascular physiology during early-stage photothrombotic stroke in neonatal piglets *in vivo*

1 Jeeun Kang[a,b,*], Xiuyun Liu[c,*], Suyi Cao[c], Steven R. Zeiler[d], Ernest M. Graham[e,f], Emad M.
2 Boctor[a,b,**], Raymond C. Koehler[c,**]

3   [a]   Laboratory for Computational Sensing and Robotics, Whiting School of Engineering, Johns
4   Hopkins University, MD 21218, United States.

5   [b]   Department of Radiology and Radiological Science, Johns Hopkins University School of
6   Medicine, MD 21287, United States.

7   [c]   Department of Anesthesiology and Critical Care Medicine, Johns Hopkins University School of
8   Medicine, MD 21287, United States.

9   [d]   Department of Neurology, Johns Hopkins University School of Medicine, MD 21205, United
10   States.

11   [e]   Division of Maternal-Fetal Medicine, Department of Gynecology-Obstetrics, Johns Hopkins
12   University School of Medicine, Baltimore, MD 21205, United States.

13   [f]   Neuroscience Intensive Care Nursery Program, Johns Hopkins University School of Medicine,
14   Baltimore, Maryland, MD 21205, United States

15   * These authors equally contributed.

16   **Corresponding authors:

17   Emad M. Boctor, Ph.D. eboctor1@jhmi.edu
18   Raymond C. Koehler, Ph.D. rkoehler@jhmi.edu

Abstract

Perinatal ischemic stroke is estimated to occur in 1/2300–1/5000 live births, but early differential diagnosis from global hypoxia-ischemia is often difficult. In this study, we tested the ability of a hand-held transcranial photoacoustic (PA) imaging to non-invasively detect a focal photothrombotic stroke (PTS) within 2 hours of stroke onset in a gyrencephalic piglet brain. 17 stroke lesions of approximately 1-cm^2 area were introduced randomly in anterior or posterior cortex via the light/dye PTS technique in anesthetized neonatal piglets ($n = 11$). The contralateral non-ischemic region served as control tissue for discrimination contrast for the PA hemoglobin metrics: HbO$_2$ saturation, total hemoglobin (tHb), and individual quantities of oxygenated and deoxygenated hemoglobin (HbO$_2$ and HbR). The PA-derived tissue HbO$_2$ saturation at 2 hours yielded a significant separation between control and affected regions-of-interest ($p < 0.0001$), which were well matched with 24-hr post-stroke cerebral infarction confirmed in the triphenyltetrazolium chloride (TTC)-stained image. The quantity of HbO$_2$ also displayed a significant contrast ($p = 0.021$), whereas tHb and HbR did not. The analysis on receiver operating characteristic curves and multivariate data analysis also agreed with the results above. This study shows that a hand-held transcranial PA neuroimaging can detect a regional thrombotic stroke in cerebral cortex of a neonatal piglet. In particular, we conclude that the HbO2 saturation metric can be used alone to identify regional stroke lesions. The lack of change in tHb may be related to arbitrary hand-held imaging configuration and/or entrapment of red blood cells within the thrombotic stroke.

Keywords: Transcranial; photoacoustic imaging; photothrombotic stroke; hemoglobin; oxygen.

Introduction

Perinatal arterial ischemic stroke is estimated to occur in 1/2300–1/5000 live births, and can result in long-term deficits in motor, cognitive, attention, and executive functions and persistent seizures [1–4]. Despite of all the efforts, there is still no effective treatment available to improve the functional recovery after perinatal stroke, and "damage control" based on a rapid detection and following neuroprotective treatment has been the best strategy in clinical use [5,6]. The traditional strategy is mainly based on a supportive care [7,8]. Several fetal monitoring technologies have been developed to enable the prompt treatment but have great limitations. Electronic fetal heart rate monitoring (EFHM) has been a standard of care in perinatal monitoring since 1970s. However, no benefit has been shown in l cerebral palsy by using EFHM, while the cesarean delivery has increased from 5% to more than 30% since using this technology [9]. Meanwhile, several studies showed that EFHM has a critical false-positive rate, even as high as 99.8 % [10], and not sensitive for perinatal stroke detection in fetal brain [11]. Magnetic resonance imaging (MRI) is the definitive diagnostic tool for ischemic stroke after birth, but its application in the newborn is questionable due to the inaccessibility in the first day after birth [12]. As alternatives, several biophotonic modalities have been proposed to allow cost-effective and continuous monitoring of neonatal brain in this period. Near-infrared spectroscopy (NIRS) and diffused optical tomography (DOT) have shown their capability of non-invasive, continuous, and fast monitoring of cerebral oxygenation level and hemodynamic changes in the neonatal brain [13,14]. However, both methods suffer from low spatial specificity and incapability of distinguishing the arterial and venous compartments, leading to low clinical specificity. Therefore, there is a critical need for effective and prompt monitoring of the perinatal brain preferably with quantitative metrics of physiological dynamics to enable early-stage decision and immediate commencement of the treatments.

Photoacoustic (PA) sensing modality, a combination of ultrasound and optical modalities, has been highlighted recently due to its high spatiotemporal resolution and deep imaging depth, which may play an alternative role for the unmet clinical need. The technology emits the pulse laser light on intact skin, and the light penetrates into deep tissue determined by the distribution of tissue scattering coefficients. After being absorbed at localized tissue with unique absorption coefficients, the conversion of absorbed energy to instantaneous heat would generate the thermal elastic expansion, which leads to pressure which is detected by an external ultrasound transducer [15]. Several clinical applications using PA technology have been proposed [16–20], and hemodynamic imaging has been a primary clinical application with stark hemoglobin absorbance, enabling quantifications of blood oxygen saturation and cerebral blood volume [21–23]. Transcranial PA sensing of physiological change at the superior sagittal sinus (SSS) has been demonstrated in the neonatal piglet and ovine models through intact scalp [24–26], but there is still room for further development to have physiological measures in brain tissue, wherein the concentration of hemoglobin is an order of magnitude less than in the sagittal sinus vein. J. Lv, *et al.* also demonstrated transcranial PA imaging of structural and functional dynamics over rodent brain during ischemic stroke at a very early stage (from 5-min to 6-hour onset) [27], but the implication for clinical translation is still limited by the use of the rodents with impractical imaging scale and small signal attenuation with its very thin skull layer.

Therefore, development of a preclinical stroke model that has a scale and maturity level comparable to human newborns is an important component for the evaluation of a novel fetal brain monitoring modality. We chose to study newborn piglets with a 40 g gyrencephalic brain in which neuroanatomical and neurophysiological features well resembling those in term human infants can be achieved [28–30] with similar brain growth and developmental patterns [30–32]. A variety of adult

85   rodent ischemic stroke models have been developed, including internal carotid arterial suture
86   occlusion of the middle cerebral artery (MCAO), direct surgical occlusion through a craniotomy,
87   direct application of endothelin-1 on the vessels, injection of an embolus, and photothrombosis in the
88   light/dye model. However, because the piglet has a rete mirablis, the internal carotid arterial suture
89   model and embolic model are not feasible [33]. On the other hand, the photothrombosis (PTS) stroke
90   model induces ischemia in a well-defined region, with minimal surgical intervention, low mortality,
91   and high reproducibility [34]. The PTS technique induces a cortical infarction through the photo-
92   activation of a light-sensitive dye (e.g., Rose bengal, erythrosin B) previously delivered into the
93   circulation, resulting in local vessel thrombosis in the areas exposed to the light [35]. This model has
94   been used successfully in the newborn piglet [28,29]. When the circulating dye is illuminated at the
95   effective wavelength, it generates free radicals that lead to endothelial damage, platelet activation,
96   and thrombosis in both pial and intraparenchymal vessels within the irradiated area [34].

97   Herein, we present transcranial PA imaging of regional ischemic stroke in the neonatal piglet
98   model.   We specifically assumed PA imaging metrics that can be achieved in a bedside diagnostic
99   setup using a hand-held PA imaging device in order to achieve a critical translational milestone
100   towards its clinical application. There are three aims of this study: (1) To establish stable regional
101   stroke models in the neonatal piglet; (2) to investigate whether ischemic features in the PA imaging,
102   such as oxyhemoglobin (HbO_2) saturation, total hemoglobin concentration (tHb), and HbO_2 and HbR
103   quantities, can contribute to an accurate localization of PTS lesions; (3) to validate whether those
104   early features obtained in 2 hours post-stroke period in a hand-held PA imaging form factor can
105   predict cerebral infarction at a later time point.

Results

107   **Photothrombotic stroke *in vivo*.** Figure 1 shows the experimental setup to induce 17 focal
108   infarctions in 11 piglets (weight 1.35 kg – 1.80 kg). In detail, 5 piglets received one PTS lesion for
109   the controlled characteristics of PA imaging PTS lesions, while the other 6 piglets received two
110   lesions to mimic the unpredictable nature of stroke induction more accurately. For the latter group,
111   the lesions were randomly selected among pre-determined four candidate positions at frontal and
112   posterior cortex regions (Figure 1c). The single-lesion group only considered the posterior cortex
113   regions. We anticipated no difference in the generation of PTS lesions depending on the cortical
114   position, following the mechanism of PTS protocol generating thrombosis in direct region of light
115   illumination. The cortical infarction width (lateral) and length (sagittal) was identified by contouring
116   the white surface area in TTC-stained brain. The PTS protocol yielded well controlled mean cortical
117   infarction area of 1 cm^2 with 0.89 ± 0.20 cm and 1.03 ± 0.41 cm of width and length (mean $\pm$ SD),
118   respectively.

119   **Transcranial PA imaging of PTS lesions in neonatal piglet *in vivo*.** Figures 1a and 1b show the
120   experimental setup and protocol for the induction of regional ischemic stroke and transcranial PA
121   imaging within 2 hours, followed by a triphenyltetrazolium chloride (TTC) staining to confirm
122   eventual development of cortical infarction at 24 hours from the stroke induction. Figure 1c shows a
123   representative TTC image, illustrating clear development of infarction via PTS technique. Dotted
124   circles indicate the candidate PTS regions, and blue and white colors indicate the affected and control
125   regions-of-interest (ROIs). Apparent regional developments of cerebral infarction were identified at
126   the regions where the PTS protocol was applied (blue dotted circles), compared to the control ROIs
127   (white dotted circles). Figure 1d shows the representative transcranial PA imaging in neonatal piglet
128   *in vivo* obtained within 2 hours from the PTS onset. The transverse image of HbO_2 saturation and tHb
129   shows the maximal and minimal intensity projection maps over 3-mm depth range in the superficial

130   cortical region. In particular, HbO_2 saturation clearly localized PTS lesions corresponding to where
131   they manifested in the TTC image (Figure 1c).   Figure 1e presents HbO_2 and HbR distributions in
132   the corresponding transverse PA image. In visual assessment, interestingly, low HbO_2 and higher
133   HbR were introduced in PTS lesions when compared to control ROIs in the contralateral sides.

134   Figure 2 and Table 1 present and summarize the quantitative measurements of HbO_2 saturation,
135   tHb, HbO_2, and HbR in the PTS model. In the piglets with a single lesion (Figure 2b), the HbO_2
136   saturation was the most obvious metric giving robust statistical significance between control and
137   affected ROIs ($p < 0.0001$, $n = 5$): $54.53 \pm 6.16\%$ vs. $21.19 \pm 4.59\%$ (mean ± SD). The metrics of tHb
138   and HbO_2 displayed trends for lower levels in the affected ROIs, but these did not attain statistically
139   effective separation with this small sample size. The values of HbR were not different between the
140   control side (1.63 ± 1.85 a.u.) and affected side (1.14 ± 0.67 a.u), although one outlier value was evident
141   with high HbR on the control side of the brain. Rejection of the case with an outlier out of standard
142   deviation still did not yield statistical significance: 0.94 ± 0.58 vs. 0.82 ± 0.45 a.u. In the piglets with
143   the induction of two PTS lesions (Figure 2c), the HbO_2 saturation was still the most effective single
144   metric ($60.01 \pm 13.46\%$ vs. $31.31 \pm 14.43\%$ in control and affected ROIs, respectively), although the
145   decrease in HbO_2 still did not attain statistical significance despite the higher sample size (12 lesions
146   in 6 piglets). The HbR concentration in the double-lesioned piglets did display the expected increase
147   in the affected ROIs when compared to those at the control ROIs: 1.27 ± 0.47 vs. 1.94 ± 0.58 in arbitrary
148   unit (a.u.), respectively ($p = 0.0045$).   Finally, we analyzed the pooled data to have a generalized
149   perspective how accurate PA imaging can detect PTS lesions (Figure 2a). The HbO_2 saturation again
150   yielded strong statistical significance: $58.40 \pm 11.86\%$ vs. $28.33 \pm 13.08\%$ in control and affected ROIs,
151   respectively. Notably, HbO_2 quantity presented a statistically significance decrease with PTS induction
152   ($p = 0.0211$). Overall, the HbR quantity did not present a statistically significant separation; however,
153   with rejection of the one outlier control value, a significant increase was observed ($p = 0.0187$). The
154   tHb concentration for the pooled data did not convey statistical significance.

155   Figure 3 shows the critical threshold for the PA imaging metrics to identify PTS lesions from
156   control ROIs. Note that the solid and dotted black lines indicate the sensitivity and specificity, and the
157   blue line indicates the accuracy. First of all, HbO_2 saturation yielded effective separation between
158   control and affected ROIs (Figure 3a), as expected from the clear statistical separation seen in Figure
159   2. We here define the effective threshold range giving sensitivity and specificity higher than 80% at
160   the same time. In the pooled data ($n = 17$), HbO_2 saturation successfully identified PTS lesions at an
161   effective threshold range between 32.48 % and 53.19%; the maximal accuracy was 91.18%. Also, the
162   PTS induction with single lesion presented with a wide effective threshold range between 23.31% and
163   53.91% ($n = 5$). Encouragingly, the maximal accuracy at 100 % was achieved between 25.95 % and
164   44.89 % of threshold range. Introduction of two PTS lesions showed a somewhat narrower effective
165   threshold range between 36.55 % and 54.40 % ($n = 12$) with the maximal accuracy of 91.67%. Figure
166   3b shows the corresponding analysis on tHb concentration threshold. In general, there were no cases
167   giving an effective threshold range. Even though the maximal accuracy of 80% was achieved with the
168   single PTS lesion cases in the range between 3.57 and 5.50 a.u., the sensitivity in that range only
169   reached 60%. The maximal accuracy was 66.67% in the cases with two PTS lesions. Pooled data also
170   showed low accuracy at 70.59%. The individual analysis on HbO_2 and HbR quantities presented
171   moderate elevation of their accuracies (Figure 3c) but still did not yield meaningful improvement
172   compared to HbO_2 saturation. The maximal accuracy ranged from 60% - 80%, and very narrow
173   effective threshold ranges were identified only with HbO_2 quantity with single-lesion case ($1.62 - 1.72$
174   a.u).

175   Figure 4 shows the receiver operating characteristic (ROC) curves for a threshold-invariant
176   evaluation of PA imaging on PTS lesion detection. Note that the dotted and solid black lines indicate

177   the ROC curves of the cases with a single-lesion ($n = 5$) and two-lesions ($n = 12$), respectively. The
178   blue line presents the ROC curve using the pooled data ($n = 17$). Table 1 also contains the area-under-
179   the-curve (AUC) measurements from the ROC curves. The HbO_2 saturation metric provided creditable
180   classification of PTS lesions with AUC values at 0.92, 1.00, and 0.89 in pooled, single-lesion, and two-
181   lesion cases, respectively. In hemoglobin quantity metrics, AUC value over 0.80 only appeared with
182   HbO_2 in the single-lesion cases and HbR in the two-lesion cases.

183   **Supervised classification of PTS lesions.** Table 3 summarizes the supervised machine learning-
184   based classification accuracy on the control and affected ROIs. Firstly, a single-variable classification
185   scenario was evaluated using individual PA imaging metrics. In general, the classification accuracy
186   followed the statistical significance presented in Figure 3, as expected. The pooled data presented the
187   maximal accuracy at 91.2% when only HbO_2 saturation was included. Meanwhile, other hemoglobin
188   quantity metrics (i.e., tHb, HbO_2, and HbR) did not present any useful classification accuracy. The
189   reduced data with single and two PTS lesions followed the same trends.   Secondly, multivariable
190   SVM models were analyzed with different number and combinations of variables. However, the
191   addition of hemoglobin quantity metrics did not benefit the accuracy over the single-variable scenario
192   solely using HbO_2 saturation metric. The maximal accuracy in the multivariable models was 88.2%
193   when used the pooled data and included HbO_2 saturation as one of the variables. The cases without
194   HbO_2 saturation only provided up to 73.5% of accuracy. The use of other classifiers in the
195   multivariable classification scenario (e.g., tree, discriminant, logistic regression, naïve bayes,
196   quadratic/cubic/Gaussian SVMs, nearest neighbor, and ensemble) did not present any improvement
197   over the single-variable classification accuracy on HbO_2 saturation (< 91.2 %), which implies that
198   none of them take advantage from tHb, HbO_2 and HbR metrics.

Discussion

200   In this paper, we demonstrate the feasibility of transcranial PA imaging of regional ischemic stroke in
201   neonatal piglets *in vivo*. We found that the HbO_2 saturation metric was sufficient for effective
202   detection in a hand-held PA imaging system. A hand-held monitoring system has clinical translation
203   potential for diagnosis of perinatal arterial ischemic stroke at the bedside. Moreover, the near-infrared
204   light could penetrate the scalp and skull of the piglet and provide a PA signal with spatial resolution
205   that was adequate for detecting an ischemic lesion on a centimeter scale. The transcranial PA
206   imaging of HbO_2 saturation may address limitations of other perinatal monitoring modalities: having
207   direct cerebral hemodynamic contrast (over EFHM); continuous and prompt monitoring (over MRI);
208   portable bedside monitoring (over MRI); and sub-millimeter-scale spatial specificity (over
209   biophotonic modalities). However, the tissue quantity of total hemoglobin did not provide additional
210   effectiveness in the context of the PTS model. There are many foreseeable variables in hemoglobin
211   quantity; for example, inconsistent distance and angle of the PA probe from the fetal head would
212   affect light fluence and acoustic attenuation. These will directly affect the estimation of hemoglobin
213   quantity in individual patients, leading to patient-to-patient variability. This limitation could be
214   mitigated by assuming that the ischemia is limited to a focal region of brain, thereby providing a
215   within-patient contrast with non-ischemic tissue.

216   It should be noted that the PTS model used here has specific hemodynamic consequences that
217   differ from embolic models. In particular, the measures of hemoglobin quantity suggested complex
218   physiologic features within the affected ROIs. The affected ROIs exhibited inconsistent decreases in
219   tHb, with as the decreases inHbO_2 coincided with increases in HbR. Thrombosis evoked by
220   endothelial damage from the light/dye interaction likely starts in venules and capillaries, where shear
221   stress is lower than in arterioles. Furthermore, because venules and capillaries have no smooth

222   muscle layer, damaging their endothelium will more readily expose underlying collagen in the
223   extracellular matrix, which activates platelets and causes leukocytes to stick to the endothelium. The
224   resulting thrombosis will cause entrapment of red blood cells within the microcirculation. This
225   entrapment may account for the inconsistent decrease in tHb reported by PA imaging in this model.
226   In contrast, embolic occlusion of a major cerebral artery reduces inflow into the microcirculation but
227   does not block outflow. Indeed, PET images of brain in adult ischemic stroke show a decrease in
228   cerebral blood volume that correlates with the decrease in cerebral blood flow [36,37]. Thus, the tHb
229   response may differ with a perinatal stroke in humans, in which a clot typically occludes large
230   cerebral arteries rather than vessels in the microcirculation. Unfortunately, the rete mirabilis between
231   the pharyngeal artery and the intracranial internal carotid artery in the pig does not permit induction
232   of a focal stroke in only a portion of the cerebral hemisphere by insertion of a blunted tip filament or
233   blood clot or by embolization with microspheres. Therefore, further investigation of PA imaging
234   capabilities in a model of embolic stroke in the piglet would likely require a full craniotomy to
235   directly occlude a major cerebral artery.

236   Several engineering strategies could be employed to improve and supplement the proposed
237   framework. The spatial resolution of the transcranial PA imaging is subject to the degree of phase
238   aberration when imaging through skull layers, having heterogenous thickness with sound propagation
239   speeds significantly different from that of soft biological tissue (4,080 m/s vs. 1,540 m/s). Even
240   though the human newborn skull is thinner than adults and more transparent at the open fontanelles,
241   the use of effective phase aberration correction will further improve the spatial resolution [38]. In
242   addition, spectral attenuation in scalp and skull layers also needs to be corrected for accurate spectral
243   unmixing [39]. 'Spectral coloring' artifacts are generated by light absorbance at fetal scalp and
244   superficial vessels containing abundant melanin and blood, resulting in lower spectral unmixing
245   accuracy due to the discrepancy between a measured PA spectrum and reference absorption spectrum
246   of hemoglobin. Even though we compensated the artifacts with *ex vivo* calibration, more advanced
247   fluence estimation and correction at individual imaging wavelengths will further improve the
248   imaging quality for accurate stroke identification.

249   Our long-term goal is to transform our transcranial PA imaging system into a safe, compact, and
250   cost-effective form factor to facilitate its clinical translation. The investigation should be based on
251   promising progress in compact light source (pulse laser diode [40], light-emitting diode [25], etc.)
252   and ultra-portable ultrasound imaging systems [41–43]. For example, monitoring of a vulnerable
253   neonate may also necessitate a compact yet effective monitoring device integrated in the neonatal
254   intensive care unit (NICU). The careful tradeoff between image quality and compactness for fluent
255   workflow would be a key for a successful clinical translation.

256   In adult stroke, early imaging with CT or MRI provides a differential diagnosis of ischemic
257   versus hemorrhagic stroke and selecting patients for treatment with tissue plasminogen activator and
258   endovascular thrombectomy [44–46]. Early imaging results also allows for selection of patients in
259   clinical trials that are most likely to benefit from therapeutic interventions. In contrast, clinical trials
260   of newborn stroke are hampered by constraints of imaging unstable newborns in the first few hours
261   after birth and the limited ability to differentiate intrapartum global hypoxia-ischemia from a focal
262   stroke based on the early neurological exam. Newborns with stroke can present with seizures by 12
263   hours after birth [11], but neuroprotectants are unlikely to have a major benefit when initiated after
264   seizure onset. Therefore, the ability to diagnose a focal stroke within a few hours after birth could
265   have a major impact by enabling early enrollment and stratification in clinical trials for early
266   treatments. Hence, noninvasive PA imaging, by differentiating focal stroke from global hypoxia-

267 ischemia, has great potential for advancing clinical trials of neonatal stroke, along with promising
268 technological progresses [47,48].

269   In conclusion, a transcranial PA imaging is capable of identifying a focal thrombotic stroke in a
270 neonatal piglet model with intact scalp and skull at an early stage before the infarction is formed.
271 Furthermore, the PA-derived HbO_2 saturation is sufficient for providing robust sensitivity and
272 specificity for detecting 1 cm focal cortical strokes. This technology has great potential for rapid and
273 early diagnosis of perinatal ischemic stroke in clinics.

Materials and Methods

275 **Photothrombotic model in neonatal piglets *in vivo*.** All procedures were approved by the Johns
276 Hopkins University Animal Care and Use Committee. Aseptic surgery was performed on male
277 piglets anesthetized with isoflurane (approximately 1.5%) during the whole procedure. The position
278 of piglet head was stabilized by using a custom stereotaxic equipment. The lungs were ventilated via
279 intubation (endotracheal tube Tube, 2.5 mm, cuffed, Medsource Labs, MN, USA) with
280 approximately 25% O_2 and 75% air. A femoral artery and a jugular vein were catheterized, and the
281 mean arterial blood pressure was continuously monitored. Rectal temperature was maintained near
282 38.0~38.5 °C with a warm blanket. Arterial pH, PCO_2, PO_2 , Hb, HbO_2 saturation, and glucose were
283 measured with a blood gas analyzer (ABL800 FLEX blood gas analyzer, Radiometer America Inc.
284 Brea, CA, USA). A fluid of 5% dextrose and 0.45% sodium chloride was infused through jugular
285 vein at the rate of 10 ml/h. Eleven male piglets, weighing 1.57 ± 0.18 kg were included in this study,
286 with 5 in the single-lesion and 6 in the two-lesion PTS groups. Their mean arterial blood pressure at
287 baseline was 61.3 ± 12.8 mmHg, and mean temperature was at 37.5 ± 0.7 °C. Blood sample data are
288 summarized in Table 2. Note that we did not make any attempt to study equal numbers of male and
289 female piglets because we are not aware of any plausible biological reason for sex differences in
290 neurovascular physiology for direct photothrombosis.

291   A solution of 20 mg/kg Rose Bengal (4,5,6,7-tetrachloro-2',4',5',7'-tetraiodofluorescein, RB) s
292 in sterile saline was injected via jugular vein. The dye has an absorbance peak at approximately 560
293 nm [49], and the skull was thinned with a drill to allow sufficient light to penetrate the cortex. The
294 focal skull areas overlying the frontal (5 mm anterior and 8 mm lateral from bregma) and posterior
295 brain tissue regions (5 mm posterior and 8 mm lateral from bregma) was thinned with 5-mm width.
296 The skull thinning was performed bilaterally, but only half of the focal areas were targeted for
297 photothrombosis. In those targeted for photothrombosis, the thinned skull was illuminated with a 5-
298 mm aperture cold-white light at the intensity of $60 - 75$ mW/cm^2 for 20 minutes. The light interaction
299 with the dye generates free radicals that damage the endothelium sufficiently to activate platelets and
300 produce a thrombus. During the light illumination, 1 ml sterile saline solution was perfused on the
301 thinned skull every 5 minutes to prevent overheating and damage on target surface. No signs of
302 thermal damage due to the light illumination were found with light illumination in the absence of
303 Rose Bengal dye with regular saline flushing.

304 **Photoacoustic imaging system and protocol.** Figure 1a shows the experimental system
305 configuration. For PA recording, 5.2-MHz clinical ultrasound linear array transducer (L7-4, ATL
306 Ultrasound Inc.) was connected to a research package (Vantage 256, Verasonics Inc., USA). Detailed
307 imaging parameters are as follows: elevation focal depth, 25 mm; element pitch, 0.30 mm; element
308 height, 7.5 mm for transducer, 18 and 24 dB low-noise amplification (LNA) settings during
309 ultrasound (US) and PA imaging. Those parameters and system configuration are available in
310 modern clinical US imaging platforms, maximizing the translationability of the research outcome

311   into clinics. To induce the PA signals, pulsed laser light was generated by a second-harmonic (532

312   nm) Nd: YAG laser pumping an optical parametric oscillator (OPO) system (Phocus Inline, Opotek

313   Inc., USA). The tunable range is 690-900 nm and the maximum pulse repetition frequency is 20 Hz.

314   Light was delivered into the probe through bifurcated fiber optic bundles, each with 40-mm long and

315   0.88-mm wide aperture. The PA probe is located on the center of piglet head along with the coronal

316   plane to simultaneously monitor the PA signal changes originated from superior sagittal sinus and

317   cerebral brain tissue. The distance between fiber bundle output and piglet head was maintained at 20

318   mm, leading to the 5 mJ/cm^2 of energy density on the skin surface. This is far below the maximum

319   permissible exposure (MPE) of skin to laser radiation guided by the ANSI Z136.1 standard, Safe Use

320   of Lasers (i.e., 20 mJ/cm^2). [54] In addition, 64 subsequent frames were averaged to overcome the

321   limited signal-to-noise ratio (SNR) at cerebral brain tissue regions with naturally less blood content

322   than the sagittal sinus and to alleviate the energy fluctuation in the Nd:YAG OPO laser source.

323   Figure 1b shows *in vivo* experimental protocol. At 20-min after inducing the last PTS,

324   translational scanning was initiated from frontal to posterior regions for volumetric PA imaging

325   within 20-30 min. The translational scanning was performed from front to the back of the brain in 1

326   mm intervals with a motorized stage (MTS50/M-Z8 and TDC001, Thorlabs Inc., USA). The HbO$_2$

327   saturation and tHb were decomposed from spectral PA data (700–900 nm in 10 nm interval), and

328   transverse planes were projected in axial direction at every 1 mm depth interval. From the data,

329   spectral unmixing was conducted by a constrained linear least-squares problem solver in MATLAB

330   software (Mathworks Inc., USA). Optical absorbance of HbO$_2$ and deoxy-Hb was obtained from

331   spectrophotometric measurement (brought from [50]). The mean spectral attenuation was measured

332   *ex vivo* and compensated before the spectral unmixing process [24].

333   **Triphenyltetrazolium chloride (TTC) staining and imaging.** After the PA scanning, the isoflurane

334   was stopped, and the piglet was carefully removed from the stereotaxic apparatus. The piglet was

335   kept on a pre-warmed heating pad until it was fully awake The pig was extubated when it regained a

336   cough reflex.. The piglet was returned to the cage and fed formula milk. On the next day, the piglet

337   was euthanized with an overdose of pentobarbial, and the brain was removed for staining with the

338   vital dye TTC (2% solution) on fresh tissue. TTC stains intact mitochondrial enzymes red whereas

339   the infarcted region in pale (Figure 1c). The surface contour of cerebral infarction carefully was

340   drawn by one of the authors (X. Liu). We correlated the PA images with 24-hr post-stroke focal

341   infarction developments on cortex detected through TTC image.

342   **Statistical analysis.** PA metrics were compared between the affected ROIs and the contralateral

343   control ROIs by paired t-test. ROC curves and corresponding AUC were reconstructed and

344   calculated in MATLAB software (R2020a, Mathworks, Inc., USA) using *perfcurve* function.

345   **Supervised machine learning.** The pooled measurements from control and affected ROIs (n = 34)

346   were fed into a supervised machine learning classification learner. Various combinations of PA

347   imaging metrics (i.e., HbO$_2$ saturation, tHb, HbO$_2$, and HbR) were trained in a linear SVM model

348   using MATLAB software (R2020a, Mathworks, Inc., USA), and tested with 34-fold cross validation

349   scheme (i.e., 33 training data and 1 test data; repeat 34 times).

350

Acknowledgements

Conflict of Interests

The authors declare no competing financial interests.

References

[1] Bosenbark D D, Krivitzky L, Ichord R, Jastrzab L and Billinghurst L 2016 Attention and executive functioning profiles in children following perinatal arterial ischemic stroke *Child Neuropsychol* **24** 1–18

[2] Chabrier S, Peyric E, Drutel L, Deron J, Kossorotoff M, Dinomais M, Lazaro L, Lefranc J, Thébault G, Dray G, Fluss J, Renaud C, Tich S N T, Group A V C du nouveau-né (AVCnn; [Neonatal S S, Darteyre S, Dégano C, Delion M, Groeschel S, Hertz-Pannier L, Husson B, Presles E, Ravel M and Vuillerot C 2016 Multimodal Outcome at 7 Years of Age after Neonatal Arterial Ischemic Stroke *J Pediatrics* **172** 156-161.e3

[3] Fluss J, Dinomais M, Kossorotoff M, Vuillerot C, Darteyre S and Chabrier S 2017 Perspectives in neonatal and childhood arterial ischemic stroke *Expert Rev Neurother* **17** 135–42

[4] Vuillerot C, Dinomais M, Marret S, Chabrier S and Debillon T 2016 Recommendations for clinical practice after neonatal arterial ischemic stroke: Clinical monitoring and early rehabilitation intervention *Ann Phys Rehabilitation Medicine* **59** e1

[5] Basu A P 2014 Early intervention after perinatal stroke: opportunities and challenges *Dev Medicine Child Neurology* **56** 516–21

[6] Gonzalez F F and Ferriero D M 2009 Neuroprotection in the Newborn Infant *Clin Perinatol* **36** 859–80

[7] Worp H B van der, Sena E S, Donnan G A, Howells D W and Macleod M R 2007 Hypothermia in animal models of acute ischaemic stroke: a systematic review and meta-analysis *Brain* **130** 3063–74

[8] Harbert M J, Tam E W Y, Glass H C, Bonifacio S L, Haeusslein L A, Barkovich A J, Jeremy R J, Rogers E E, Glidden D V and Ferriero D M 2011 Hypothermia Is Correlated With Seizure Absence in Perinatal Stroke *J Child Neurol* **26** 1126–30

[9] Nelson K B, Sartwelle T P and Rouse D J 2016 Electronic fetal monitoring, cerebral palsy, and caesarean section: assumptions versus evidence *Bmj* **355** i6405

[10] Hirsch E 2019 Electronic Fetal Monitoring to Prevent Fetal Brain Injury: A Ubiquitous Yet Flawed Tool *Jama* **322** 611–2

384 [11] Adami R R, Grundy M E, Poretti A, Felling R J, Lemmon M and Graham E M 2016
385 Distinguishing Arterial Ischemic Stroke From Hypoxic–Ischemic Encephalopathy in the Neonate at
386 Birth *Obstetrics Gynecol* **128** 704–12

387 [12] Gunn A J, Bennet L, Gunning M I, Gluckman P D and Gunn T R 1999 Cerebral Hypothermia Is
388 Not Neuroprotective When Started after Postischemic Seizures in Fetal Sheep *Pediatr Res* **46** 274–80

389 [13] Lee C W, Cooper R J and Austin T 2017 Diffuse optical tomography to investigate the newborn
390 brain *Pediatr Res* **82** 376–86

391 [14] Semyachkina-Glushkovskaya O V, Kurths J, Pavlov A N, Borisova E G, Abdurashitov A S, Zhu
392 D, Li P, Luo Q and Tuchin V V 2016 Silent Vascular Catastrophes in the Brain in Term Newborns:
393 Strategies for Optical Imaging *Ieee J Sel Top Quant* **22** 88–101

394 [15] Wang L V and Hu S 2012 Photoacoustic Tomography: In Vivo Imaging from Organelles to
395 Organs *Science* **335** 1458–62

396 [16] Yao J, Maslov K I and Wang L V 2012 In vivo Photoacoustic Tomography of Total Blood Flow
397 and Potential Imaging of Cancer Angiogenesis and Hypermetabolism *Technol Cancer Res T* **11** 301–
398 7

399 [17] Kang J, Chang J H, Kim S M, Lee H J, Kim H, Wilson B C and Song T-K 2017 Real-time
400 sentinel lymph node biopsy guidance using combined ultrasound, photoacoustic, fluorescence
401 imaging: in vivo proof-of-principle and validation with nodal obstruction *Sci Rep-uk* **7** 45008

402 [18] Kang J, Kim E, Kim G R, Yoon C, Song T and Chang J H 2015 Photoacoustic imaging of breast
403 microcalcifications: A validation study with 3-dimensional ex vivo data and spectrophotometric
404 measurement *J Biophotonics* **8** 71–80

405 [19] Kang J, Zhang H K, Kadam S D, Fedorko J, Valentine H, Malla A P, Yan P, Harraz M M, Kang
406 J U, Rahmim A, Gjedde A, Loew L M, Wong D F and Boctor E M 2019 Transcranial Recording of
407 Electrophysiological Neural Activity in the Rodent Brain in vivo Using Functional Photoacoustic
408 Imaging of Near-Infrared Voltage-Sensitive Dye *Front Neurosci-switz* **13** 579

409 [20] Kang J, Kadam S D, Elmore J S, Sullivan B J, Valentine H, Malla A P, Harraz M M, Rahmim
410 A, Kang J U, Loew L M, Baumann M H, Grace A A, Gjedde A, Boctor E M and Wong D F 2020
411 Transcranial photoacoustic imaging of NMDA-evoked focal circuit dynamics in the rat hippocampus
412 *J Neural Eng* **17** 025001

413 [21] Li M, Tang Y and Yao J 2018 Photoacoustic Tomography of Blood Oxygenation: A Mini
414 Review *Photoacoustics* **10** 65–73

415 [22] Hu S and Wang L V 2010 Neurovascular Photoacoustic Tomography *Frontiers Neuroenergetics*
416 **2** 10

417 [23] Hu S 2016 Listening to the Brain With Photoacoustics *Ieee J Sel Top Quant* **22** 117–26

[24] Kang J, Boctor E M, Adams S, Kulikowicz E, Zhang H K, Koehler R C and Graham E M 2018 Validation of noninvasive photoacoustic measurements of sagittal sinus oxyhemoglobin saturation in hypoxic neonatal piglets *J Appl Physiol* **125** 983–9

[25] Kang J, Koehler R C, Adams S, Graham E M and Boctor E M 2020 Light-emitting diode-based transcranial photoacoustic measurement of sagittal sinus oxyhemoglobin saturation in hypoxic neonatal piglets *Biorxiv* **262451** 2020.08.22.262451

[26] Petrova I Y, Petrov Y Y, Esenaliev R O, Deyo D J, Cicenaite I and Prough D S 2009 Noninvasive monitoring of cerebral blood oxygenation in ovine superior sagittal sinus with novel multi-wavelength optoacoustic system *Opt Express* **17** 7285

[27] Lv J, Li S, Zhang J, Duan F, Wu Z, Chen R, Chen M, Huang S, Ma H and Nie L 2020 In vivo photoacoustic imaging dynamically monitors the structural and functional changes of ischemic stroke at a very early stage *Theranostics* **10** 816–28

[28] Armstead W M, Riley J, Kiessling J W, Cines D B and Higazi A A-R 2010 Novel plasminogen activator inhibitor-1-derived peptide protects against impairment of cerebrovasodilation after photothrombosis through inhibition of JNK MAPK *Am J Physiology-regulatory Integr Comp Physiology* **299** R480–5

[29] Armstead W M, Ganguly K, Riley J, Zaitsev S, Cines D B, Higazi A A-R and Muzykantov V R 2012 RBC-coupled tPA Prevents Whereas tPA Aggravates JNK MAPK-Mediated Impairment of ATP- and Ca-Sensitive K Channel-Mediated Cerebrovasodilation After Cerebral Photothrombosis *Transl Stroke Res* **3** 114–21

[30] Dobbing J and Sands J 1979 Comparative aspects of the brain growth spurt *Early Hum Dev* **3** 79–83

[31] Conrad M S, Dilger R N and Johnson R W 2012 Brain Growth of the Domestic Pig (Sus scrofa) from 2 to 24 Weeks of Age: A Longitudinal MRI Study *Dev Neurosci-basel* **34** 291–8

[32] Sheng H Z, Rosbo N K, Carnegie P R and Bernard C C A 1989 Developmental Study of Myelin Basic Protein Variants in Various Regions of Pig Nervous System *J Neurochem* **52** 736–40

[33] McColl B W, Carswell H V, McCulloch J and Horsburgh K 2004 Extension of cerebral hypoperfusion and ischaemic pathology beyond MCA territory after intraluminal filament occlusion in C57Bl/6J mice *Brain Res* **997** 15–23

[34] Kleinschnitz C, Fluri F and Schuhmann M 2015 Animal models of ischemic stroke and their application in clinical research *Drug Des Dev Ther* **Volume 9** 3445–54

[35] Labat-gest V and Tomasi S 2013 Photothrombotic Ischemia: A Minimally Invasive and Reproducible Photochemical Cortical Lesion Model for Mouse Stroke Studies *J Vis Exp*

[36] Powers W J, Grubb R L and Raichle M E 1984 Physiological responses to focal cerebral ischemia in humans *Ann Neurol* **16** 546–52

453   [37] Powers W J, Grubb R L, Darriet D and Raichle M E 1985 Cerebral Blood Flow and Cerebral
454   Metabolic Rate of Oxygen Requirements for Cerebral Function and Viability in Humans *J Cereb*
455   *Blood Flow Metabolism* **5** 600–8

456   [38] Wang L V 2008 Prospects of photoacoustic tomography *Med Phys* **35** 5758–67

457   [39] Cox B, Laufer J G, Arridge S R and Beard P C 2012 Quantitative spectroscopic photoacoustic
458   imaging: a review *J Biomed Opt* **17** 0612021–06120222

459   [40] Esenaliev R O 2017 Optoacoustic diagnostic modality: from idea to clinical studies with highly
460   compact laser diode-based systems *J Biomed Opt* **22** 091512–091512

461   [41] Kang J, Yoon C, Lee J, Kye S-B, Lee Y, Chang J H, Kim G-D, Yoo Y and Song T-K 2016 A
462   System-on-Chip Solution for Point-of-Care Ultrasound Imaging Systems: Architecture and ASIC
463   Implementation *Ieee T Biomed Circ S* **10** 412–23

464   [42] Kim G-D, Yoon C, Kye S-B, Lee Y, Kang J, Yoo Y and Song T-K 2012 A Single FPGA-Based
465   Portable Ultrasound Imaging System for Point-of-Care Applications *Ieee Transactions Ultrasonics*
466   *Ferroelectr Freq Control* **59** 1386–94

467   [43] Kang J, Kim P, Yoon C, Yoo Y and Song T-K 2020 Efficient Parallel-Beamforming Based on
468   Shared FIFO for Ultra-Compact Ultrasound Imaging Systems *Ieee Access* **8** 80490–501

469   [44] French B R, Boddepalli R S and Govindarajan R 2016 Acute Ischemic Stroke: Current Status
470   and Future Directions. *Mo Med* **113** 480–6

471   [45] Saver J L, Fonarow G C, Smith E E, Reeves M J, Grau-Sepulveda M V, Pan W, Olson D M,
472   Hernandez A F, Peterson E D and Schwamm L H 2013 Time to Treatment With Intravenous Tissue
473   Plasminogen Activator and Outcome From Acute Ischemic Stroke *Jama* **309** 2480–8

474   [46] Meretoja A, Keshtkaran M, Saver J L, Tatlisumak T, Parsons M W, Kaste M, Davis S M,
475   Donnan G A and Churilov L 2018 Stroke Thrombolysis *Stroke* **45** 1053–8

476   [47] Nie L, Cai X, Maslov K, Garcia-Uribe A, Anastasio M A and Wang L V 2012 Photoacoustic
477   tomography through a whole adult human skull with a photon recycler *J Biomed Opt* **17** 110506–
478   110506

479   [48] Ovsepian S V, Olefir I and Ntziachristos V 2019 Advances in Optoacoustic Neurotomography
480   of Animal Models *Trends Biotechnol* **37** 1315–26

481   [49] Watson B D, Dietrich W D, Busto R, Wachtel M S and Ginsberg M D 1985 Induction of
482   reproducible brain infarction by photochemically initiated thrombosis *Ann Neurol* **17** 497–504

483   [50] Prahl S 1999 Optical Absorption of Hemoglobin

484

485

Tables

Table 1. Photoacoustic (PA) imaging metrics of photothrombotic (PTS) model *in vivo*. Asterisk marks indicate the statistical significance between the control and affected regions-of-interest (ROIs). Asterisk marks indicate statistical significance: * ($p \leq 0.05$), ** ($p \leq 0.01$), *** ($p \leq 0.001$), and **** ($p \leq 0.0001$).

	HbO$_2$ saturation (%)	Total Hb (tHb) concentration (a.u.)	HbO$_2$ concentration (a.u.)	HbR concentration (a.u.)
Pooled data (n = 17 from 11 animals)				
Control	58.40 ± 11.86	5.83 ± 3.04	4.46 ± 2.46	1.38 ± 1.02
Affected	28.33 ± 13.08	4.44 ± 2.10	2.72 ± 1.61	1.71 ± 0.70
p	< 0.0001 (****)	0.0733	0.0066 (*)	0.2314 (p = 0.0118 when n = 16 excluding an outlier, *)
AUC	0.9204	0.6540	0.7093	0.7128
Single PTS lesion (n = 5 from 5 animals)				
Control	54.53 ± 6.16	5.67 ± 4.42	4.03 ± 2.84	1.63 ± 1.85
Affected	21.19 ± 4.59	2.44 ± 1.22	1.29 ± 0.64	1.14 ± 0.67
p	0.0019 (**)	0.1070	0.0720	0.4817
AUC	1.0000	0.7200	0.8000	0.5200
Two PTS lesions (n = 12 from 6 animals)				
Control	60.01 ± 13.46	5.90 ± 2.51	4.64 ± 2.40	1.27 ± 0.47
Affected	31.31 ± 14.43	5.27 ± 1.80	3.32 ± 1.52	1.94 ± 0.58
p	< 0.0001 (****)	0.4103	0.0586	0.0128 (**)
AUC	0.8889	0.6111	0.6875	0.8403

Table 2. The arterial blood sample analysis of the piglets during stroke induction experiment (Data format: Mean ± SD). Abbreviations: pCO$_2$, Arterial carbon dioxide partial pressure; pO$_2$, Arterial oxygen partial pressure; cBase, Base excess; ctHb, Total hemoglobin; Glu, Glucose; Lac, Lactate.

pH	pCO$_2$ (mmHg)	pO$_2$ (mmHg)	cBase (mmol/L)	HbO$_2$ saturation (%)	ctHb (g/dL)
7.37 ± 0.09	37.1 ± 5.5	143.5 ± 23.6	-3.5 ± 3.3	99.7% ± 0.5%	11.0 ± 2.9
K+ (mmol/L)	Na+ (mmol/L)	Ca2+ (mmol/L)	Cl- (mmol/L)	Glu (mg/dL)	Lac (mmol/L)
3.7 ± 0.6	141.9± 3.4	1.3 ± 0.2	108.7 ± 5.1	141.9 ± 49.6	4.5 ± 8.6

495 **Table 3.** Supervised machine learning-based differential classification accuracy using a linear support vector
496 machine (SVM) classifier. 34 data points (17 ROIs for both controlled and PTS lesions) were used with 34-
497 fold cross-validation. Gray shadings indicate the variables used.

#Variables		Variables used				Accuracy (%)		
		HbO$_2$ saturation	tHb	HbO$_2$	HbR	Pooled data	Single PTS lesion	Two PTS lesions
Single-variable scenario	1	▦				**91.2**	**100.0**	**87.5**
			▦			55.9	50.0	54.2
				▦		61.8	80.0	58.3
					▦	61.8	0.0	75.0
Multi-variable scenario	2	▦	▦			88.2	90.0	87.5
		▦		▦		88.2	90.0	87.5
		▦			▦	88.2	100.0	87.5
			▦	▦		73.5	80.0	79.2
			▦		▦	73.5	80.0	75.0
				▦	▦	73.5	80.0	75.0
	3	▦	▦	▦		88.2	90.0	87.5
		▦	▦		▦	88.2	90.0	87.5
		▦		▦	▦	88.2	90.0	87.5
			▦	▦	▦	73.5	80.0	75.0
	4	▦	▦	▦	▦	88.2	90.0	87.5

498
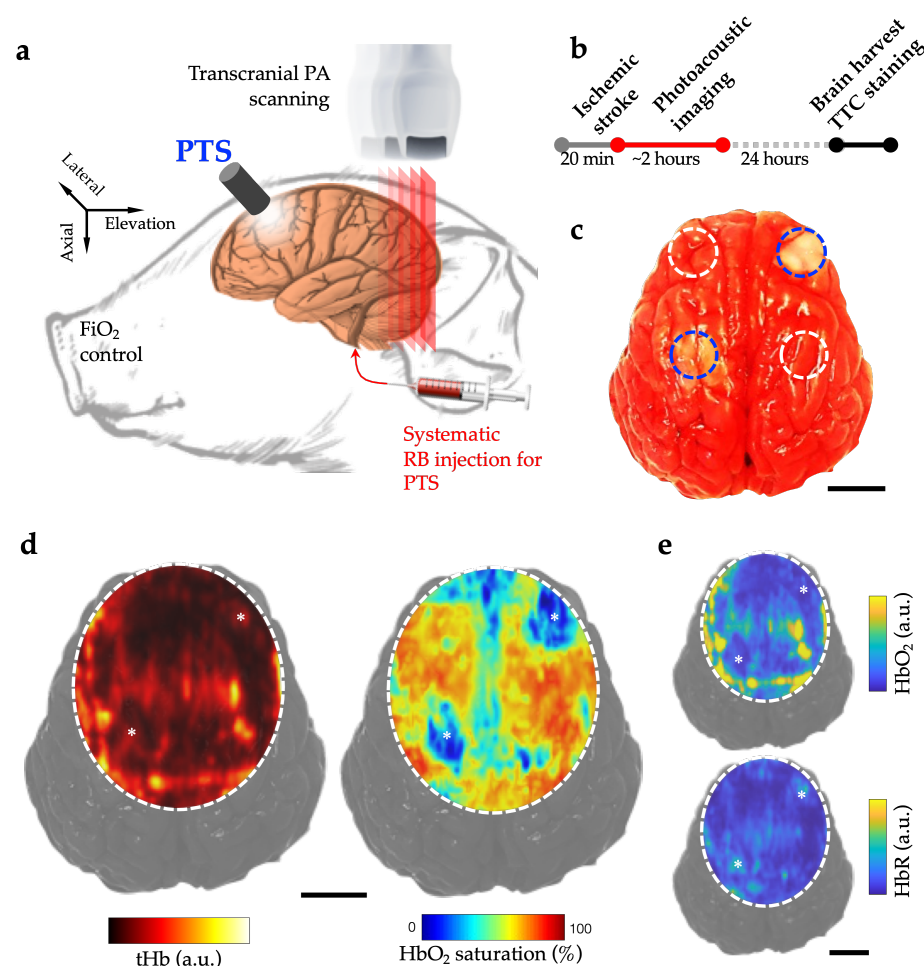
499 **Figures**

500
501 **Figure 1. The transcranial PA imaging of photothrombotic stroke in neonatal piglets *in vivo*.** (a)
502 Experimental setup and (b) protocol for PTS induction and PA imaging. (c) Triphenyltetrazolium chloride
503 (TTC) image of harvested whole brain, indicating cerebral infarction developed at 24-hr post-stroke time
504 point. Blue and white dotted circles indicate the PTS lesions and control regions-of-interest. (d) Representative
505 transverse planes of HbO_2 saturation, total hemoglobin (tHb) overlaid on the TTC image. (e) Corresponding
506 transverse maps of HbO_2 and HbR quantities. Black bars indicate 1 cm. Asterisk marks indicate the cortical
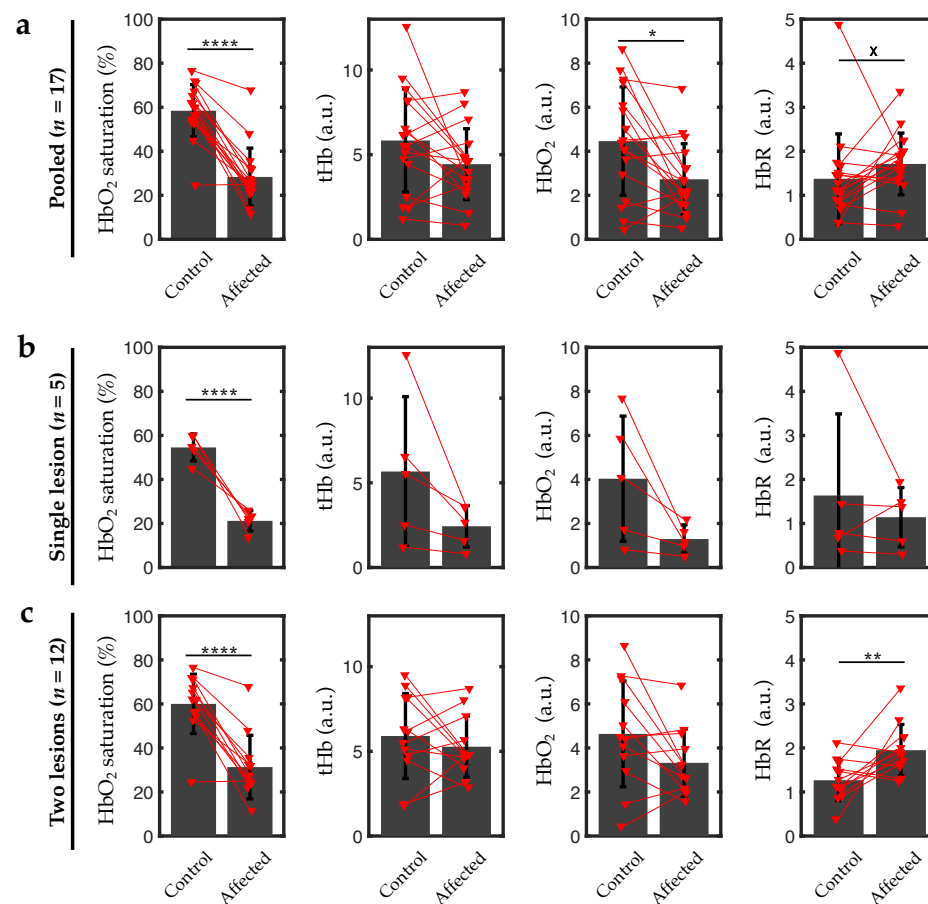507 regions presented cerebral infarction in TTC image.

508

509

Figure 2. Quantitative measurements of PA imaging metrics, HbO_2 saturation, total hemoglobin (tHb), oxyhemoglobin (HbO_2), and deoxyhemoglobin (HbR). (a) Pooled group ($n = 17$). (b) Single-lesion group ($n = 5$). (c) Two-lesion group ($n = 12$). Red indicators show the individual data points from the regions-of-interest (ROI). Red lines indicate the control and affected ROIs from individual piglets. Asterisk marks indicate the degree of statistical significance in paired t test: * ($p \leq 0.05$), ** ($p \leq 0.01$), *** ($p \leq 0.001$), and **** ($p \leq 0.0001$). X indicates a statistical significance in a specific case when removed one outlier animal data ($n = 16$, $p \leq 0.05$).
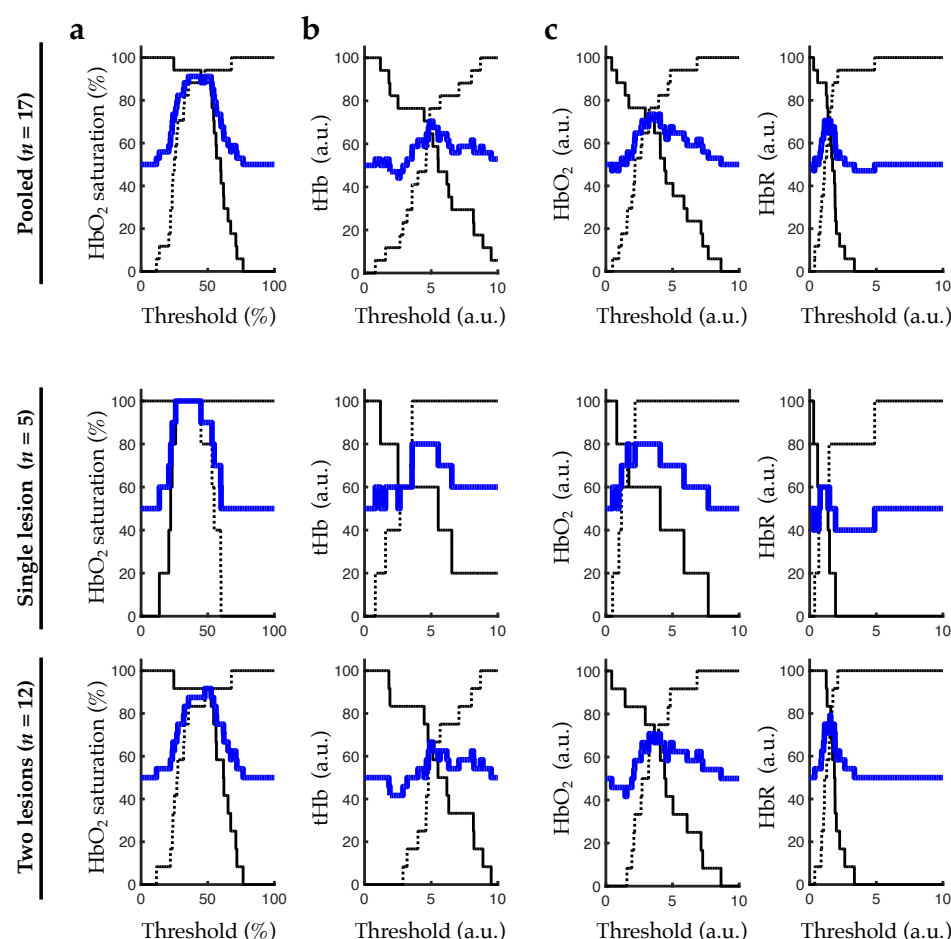
517

17

518

Figure 3. Sensitivity, specificity, and accuracy to classify the photothrombotic (PTS) lesions for the varying threshold values. (a) HbO$_2$ saturation, (b) total hemoglobin (tHb), and (c) oxy- and deoxyhemoglobin (HbO$_2$ and HbR) in pooled, single-lesion, and two-lesion groups. Solid and dotted black lines indicate specificity and sensitivity, respectively. Blue line indicates the accuracy.
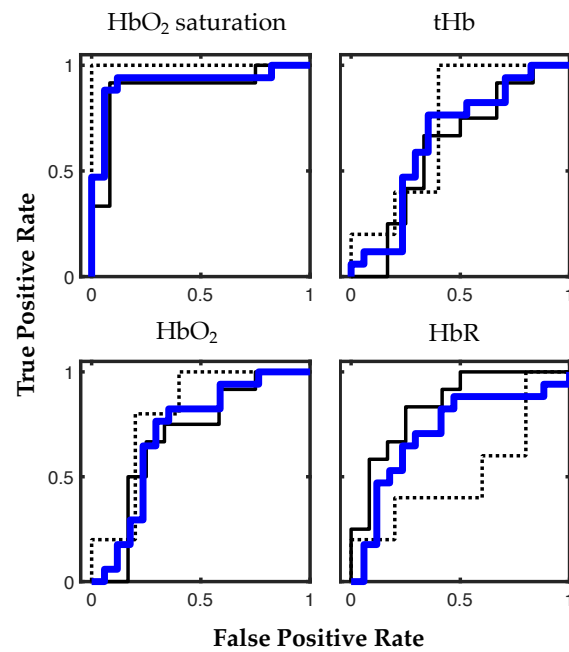
523

524

Figure 4. Receiver operating characteristic (ROC) curves for a threshold-invariant evaluation of PA imaging on PTS lesion detection. Blue line indicates the ROC curve with the pooled data. Dotted and solid black lines indicate the curves in the single-lesion and two-lesion groups, respectively.

528